Mechanisms of Surface-Mediated DNA Hybridization

Jon H. Monserud and Daniel K. Schwartz*

Department of Chemical and Biological Engineering, University of Colorado Boulder, Boulder, Colorado 80309, United States

ABSTRACT Single-molecule total internal reflection fluorescence microscopy was employed in conjunction with resonance energy transfer (RET) to observe the dynamic behavior of donor-labeled ssDNA at the interface between aqueous solution and a solid surface decorated with complementary acceptor-labeled ssDNA. At least 100 000 molecular trajectories were determined for both complementary strands and negative control ssDNA. RET was used to identify trajectory segments corresponding to the hybridized state. The vast majority of molecules from solution adsorbed nonspecifically to the surface, where a brief two-dimensional search was performed with a 7% chance of hybridization. Successful hybridization events occurred with a characteristic search time of ~0.1 s, and unsuccessful searches resulted in desorption from the surface, ultimately repeating the adsorption and search process. Hybridization was reversible, and two distinct modes of melting (*i.e.*, dehybridization) were observed, corresponding to long-lived (~15 s) and short-lived (~1.4 s) hybridized time intervals. A strand that melted back onto the surface could rehybridize after a brief search or desorb from the interface. These mechanistic observations provide guidance for technologies that involve DNA interactions in the near-surface region, suggesting a need to design surfaces that both enhance the complex multidimensional search process and stabilize the hybridized state.

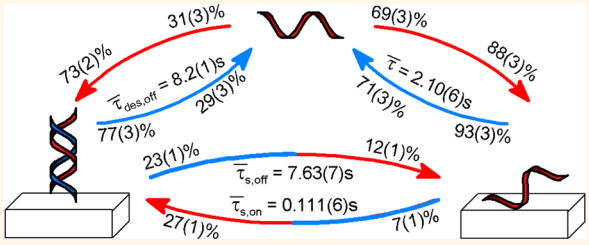

KEYWORDS: single molecule · resonance energy transfer · DNA · hybridization · molecular searching

Surface hybridization involves a *target* single-stranded DNA (ssDNA) engaging in specific interactions (hybridization) with immobilized *probe* ssDNA molecules. Various technologies rely on measurements of surface hybridization to sequence DNA,[1] to detect DNA polymorphism,[2,3] for DNA mapping,[4] and to detect DNA mutation.[5] In principle, hybridization relies on the thermodynamic equilibrium of hybridized and unhybridized DNA. The complex mechanisms behind this equilibrium involve molecular, electrostatic, and conformational interaction phenomena.[6] The complexity of hybridization is exacerbated when considering hybridization between free and immobilized DNA at an interface where probe coverage[7] and surface chemistry[8] must be considered.

While the influence of the vicinal surface is sometimes neglected, it is intuitively reasonable that the desired *specific* molecular-recognition interactions must compete with *nonspecific* interactions between probe or target molecules and the surface itself. Therefore, the physicochemical properties of the adjacent surface are hypothesized to have a significant impact on the efficiency and kinetics of hybridization and other biomolecular interactions. For example, it was found that the conformation of hairpin DNA was greatly perturbed at both hydrophobic and hydrophilic surfaces relative to solution and that the hairpin state was more stable on the hydrophobic than on the hydrophilic surface.[9] The rates of folding and unfolding were also significantly slowed at the surface.

While it is clear that hybridization at a surface is not identical to hybridization in solution, a detailed understanding of surface-mediated hybridization is lacking. Rates of hybridization on surfaces modified with DNA have been shown to depend on probe length,[10] design,[11] and surface density.[7,12−15] Classical models that describe the rate of surface hybridization based on a combination of "specific adsorption" (direct adsorption to immobilized nucleotides) and "nonspecific adsorption" (adsorption to the surface and subsequent surface transport) have been described.[16,17] In these models, target molecules may nonspecifically adsorb to the surface and undergo a two-dimensional search of the surface for an immobilized complement. Also, the target molecules may adsorb,

* Address correspondence to daniel.schwartz@colorado.edu.

Received for review December 18, 2013 and accepted April 7, 2014.

Published online April 07, 2014
10.1021/nn4064874

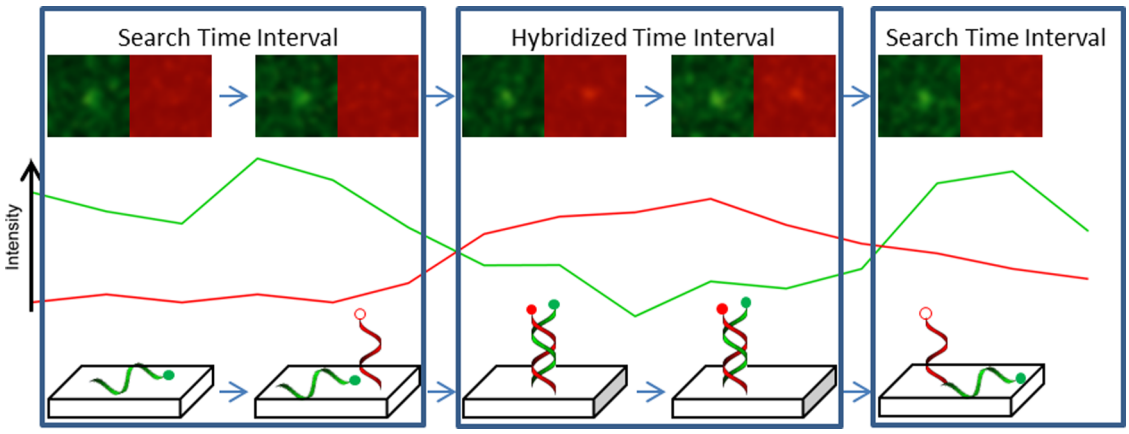

Figure 1. (Top) Raw data images, (middle) donor and acceptor emission intensity, (bottom) physical interpretation of observations. In all parts of the figure, donor fluorophores are represented in green and acceptor fluorophores in red.

diffuse, and desorb without ever hybridizing. Thus, the net rate of surface-mediated hybridization may include both the rate and efficiency associated with the search process, as well as the fundamental hybridization rate constant. It has been suggested that the two-dimensional nature of the search may enhance the flux of targets to probe sites,[17] resulting in more efficient hybridization. In fact, search processes in reduced dimensionality are generally believed to improve targeting efficiency[18−21] and are well-represented in biological systems.

Ensemble-averaging methods, such as cyclic voltammetry,[22] quartz crystal microbalance,[10] and surface plasmon resonance spectroscopy,[23] are commonly used to evaluate the *net* rate of hybridization on ssDNA arrays, but are insensitive to the mechanistic details of surface-mediated hybridization. In fact, generally these techniques do not explicitly distinguish between specific and nonspecific binding. Single-molecule (SM) methods have the potential to separate and identify competing mechanisms, like those described above, by providing detailed information about large numbers of molecular trajectories, as opposed to the ensemble average. Total internal reflection fluorescence microscopy (TIRFM) provides the requisite surface sensitivity. When coupled with intermolecular resonance energy transfer (RET), TIRFM represents an analysis tool that can evaluate the entire pathway to hybridization. In particular, the nanometer-scale range of RET provides a means to unambiguously identify hybridization events. Here it is shown that SM-RET-TIRFM can provide uniquely detailed information about the mechanisms of DNA hybridization in the near-surface environment.

RESULTS AND DISCUSSION

Spatial information in fluorescence imaging was acquired *via* resonance energy transfer. This technique involves the nonradiative energy transfer from a donor fluorophore to an acceptor fluorophore that occurs when the two fluorophores are within 1−10 nm.[24] In our experiments, amine-modified ssDNA labeled with the acceptor fluorophore was attached to an epoxide-modified silica surface. Aqueous solutions (1× PBS, pH = 7.4) of the donor-labeled complementary strand were prepared. Dual-channel image sequences were acquired of the RET-labeled complementary strands at the interface between ssDNA-modified silica and aqueous solution. Over 600 000 molecular trajectories were determined for the complementary strands; however, molecules that resided on the surface for 100 ms (1 frame) or less were removed from the analysis. Figure 1 illustrates the process used to identify RET events that indicated hybridization. The presence of objects simultaneously identified within 2 pixels (455 nm) in both donor and acceptor channels was identified as a RET event (Figure 1, top). The position of a RET event was identified using the channel with greatest signal-to-noise ratio. Fluorescence intensity was monitored in both channels for each molecular trajectory (Figure 1, middle). We identified whether a molecule was "searching" or "hybridized" by the relative distance between donor and acceptor fluorophores, $d = (F_D/F_A)^{1/6}$, where F_A and F_D are the fluorescence intensities of acceptor and donor species, respectively. The relative distance between donor and acceptor fluorophores relates to RET efficiency (E) by the following expression, $E = 1/(1 + d^6)$. A detailed derivation and discussion of these parameters is described in the Experimental Details.

Identification of Searching and Hybridized States. It was hypothesized that hybridized oligonucleotides could be distinguished from searching oligonucleotides using an appropriate criterion (a "threshold") based on RET efficiency (E) or, equivalently, a sufficiently low value of the relative donor−acceptor distance, d. In order to verify the presence of these distinct states and to establish appropriate criteria for distinguishing states, statistical distributions of all observed d values were created for all trajectories in a given experiment

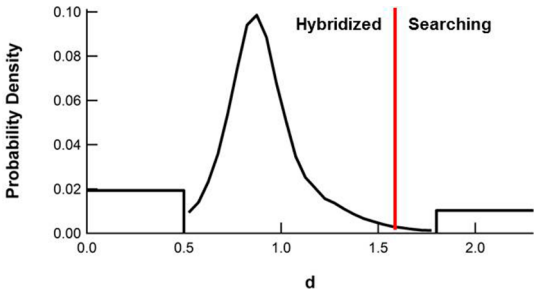

Figure 2. Distribution of the relative donor−acceptor distance for all RET observations in experiments involving complementary DNA at 293 K.

(Figure 2). In Figure 2, three distinct populations were observed, zero-RET, high-RET, and complete-RET. The extreme d values of zero-RET and complete-RET observations could not be determined quantitatively. Zero-RET occurred in the limit where the distance between donor and acceptor fluorophores was so large that an extremely large d value (low RET efficiency) was observed. This population is represented by the large bin for $d > 1.8$ (equivalent RET efficiency, $E < 0.03$) in Figure 2. Physically, this relatively small population corresponded to searching (unhybridized) donor-labeled target molecules appearing in only the donor channel. Similarly, a small population for complete-RET was resolved for $d < 0.5$ ($E > 0.98$), shown as a single bin in Figure 2, corresponding to the population that appeared only in the acceptor channel. The final population was indicated by the prominent peak centered at $d = 0.9$ ($E = 0.65$) with the range $0.5 < d < 1.8$. As discussed below, this central peak is consistent with expectations for the nominal hybridized state.

To calculate the theoretically expected RET efficiency for the hybridized state, one must consider the structural details of the labeling, including the presence of flexible linkers used to tether the fluorophores to the DNA. A three-dimensional self-avoiding random walk was used to approximate the length, and the variance of the length, of each fluorophore/linker combination. Using these lengths, along with the diameter of the dsDNA to which the linkers were attached, the approximate donor−acceptor distance was calculated to be 4.4 nm, which equates to $d = 0.81$ ($E = 0.78$) with a variance $\sigma^2 = 0.12$.[25] Notably, these values are consistent with the position and width of the central peak in Figure 2, suggesting that this central peak represents the population of nominally hybridized molecules. A similar distribution of d values was determined for experiments with noncomplementary poly-A control target molecules; this distribution is shown in Supporting Information Figure S1. The poly-A distribution exhibited a small number of RET events for values of d in the range 1.5−1.6 ($E = 0.08$−0.06), presumably due to incidental RET interactions.

The choice of the hybridization threshold criterion involved a compromise between two opposing

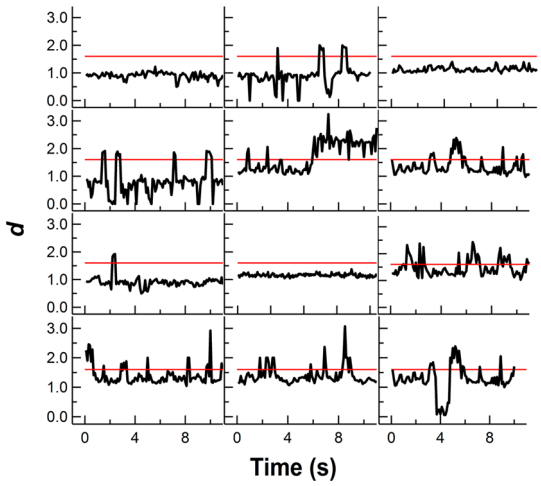

Figure 3. Representative molecular trajectories. The red lines denote the criterion defined as the threshold for hybridization, *i.e.*, $d > 1.6$ indicates a freely diffusing (searching) target molecule, while $d < 1.6$ indicates close proximity between target and immobilized probe.

considerations. By selecting a lower hybridization threshold, the risk of capturing incidental RET and RET due to noise was minimized. However, an artificially low value for the hybridization threshold would lead to identification of false searching states, where the duplex may actually be "peeling" briefly but not truly dissociating. To address this issue, the data set, using the complementary probe ssDNA, was mined for events where molecules underwent an apparent "fluctuation", involving hybridization, dehybridization, and rehybridization in successive frames. Rehybridization was identified when a molecule hybridized in ≤200 ms following dehybridization. A sensitivity analysis was performed where the hybridization threshold was systematically increased from 0 to 100 (Figure S2). As expected, the fluctuations reached a maximum at $d = 0.9$ ($E = 0.65$), matching the maximum of the d distribution peak. In the range of $d = 1.6$−2.0 ($E = 0.06$−0.02) fluctuations varied by less than 10% from the number of fluctuations at $d \geq 10$ ($E \leq 10^{-6}$). Based on these observations, a criterion was defined where the threshold between the searching and hybridized states was defined as $d = 1.6$. While this choice was somewhat arbitrary, and a different threshold would result in small changes to some numerical values reported below (*e.g.*, the number of hybridization events), the main conclusions of this paper were found to be robust with respect to small variations in the hybridization threshold criterion.

Phenomenology and Statistics of Hybridization and Melting. The criterion described above allowed us to identify molecular association events on the basis of RET efficiency; this was further used to identify dynamic transitions between searching and hybridized states from RET trajectories. Figure 3 shows a number of representative trajectories, where the $d = 1.6$ criterion

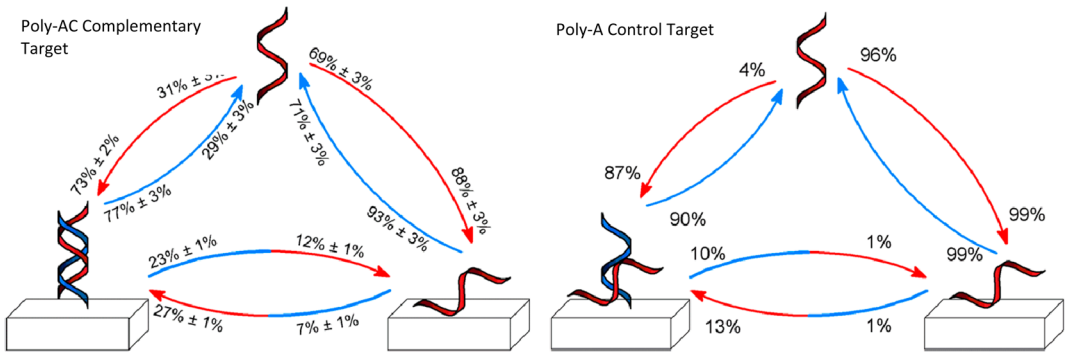

Figure 4. Fractional pathway for DNA surface hybridization. (Left) Poly-AC complementary strand; (right) poly-A control. An arrow pointing to a state (searching, hybridized, in solution) represents the percentage of molecules entering that state. An arrow leaving a state represents the percentage of molecules leaving that state.

is indicated by a solid red line. In each trajectory, a given donor-labeled target molecule was followed over time as it initially adsorbed and then proceeded to diffuse on the surface, sometimes hybridizing and/or melting (possibly multiple times), and eventually desorbing from the surface. Time intervals where $d < 1.6$ represented periods of time where the target was in close proximity (possibly hybridized) to an acceptor-labeled immobilized probe molecule. As indicated in Figure 3, molecular trajectories were highly varied. In some cases the initial observation was for $d > 1.6$, indicating adsorption into an unhybridized (searching) state. However, for other trajectories, RET was observed immediately upon adsorption ($d < 1.6$), suggesting adsorption in very close proximity to an acceptor-labeled probe. Trajectories subsequently exhibited diverse behavior, including transitions between searching and hybridized states (the d value crosses the red line) and desorption back into solution (complete loss of a given object in both spectral channels).

Approximately 600 000 individual trajectories were determined for complementary donor-labeled target molecules and for control target molecules consisting of donor-labeled poly-A. For target molecules with a complementary sequence to the probe, ~40% of trajectories (~250 000) exhibited at least one significant RET event with $d < 1.6$, while RET was observed for only ~6% of trajectories for the control poly-A oligonucleotide target. This suggested that the majority of RET events for the complementary target did in fact represent hybridization. The time-averaged hybridized fraction was calculated by integrating the overall distribution of RET efficiency and determined to be 21%. As expected, this hybridized fraction observed on the surface was significantly smaller than what would be observed in solution for molecules of similar length and composition (<80% hybridized).[26] The significantly smaller hybridization fraction at the solid–liquid interface is consistent with results of DNA hairpin surface behavior, where DNA–surface interactions tended to destabilize the DNA duplex.[27] The 6% of RET events associated with the control poly-A target had a mean duration of only 0.1 s (the acquisition time of a single "frame"), consistent with the hypothesis that these RET events represented incidental proximity during random target diffusion. As discussed in detail below, the temporal statistics of RET events for complementary target molecules were significantly different and included long-lived associations.

The molecular trajectories that exhibited apparent hybridization (~40% of all observed species) were segmented into "searching" and "hybridized" states on the basis of d as described above; each trajectory was also assumed to begin and end with an "in-solution" state. The transition from the "in-solution" state was identified by a molecule adsorbing to the surface, which was indicated by a molecule's initial appearance in the field of view. Desorption into the "in-solution" state was associated with the disappearance of a molecule from the field of view.

Transitions between the three states were enumerated and normalized by the destination or source state for both the complementary target and control sequence to determine the relative likelihoods (fractional pathways) of these various transitions. A more detailed discussion can be found in the Experimental Details. This process was performed for several temperatures over the range 293–313 K (Supporting Information Figure S3). A paired Student's t analysis revealed that all fractions were statistically identical as a function of temperature, suggesting that the fractional pathways to hybridization were insensitive to temperature over the range 293–313 K. Therefore, the fraction associated with each transition was averaged across the temperature range and shown as percentages in Figure 4. As discussed below, the temporal behavior associated with transitions between states did exhibit a systematic trend with temperature.

Analysis of the pathways to hybridization in Figure 4 shows that 31% of complementary target molecules adsorbing to the DNA-modified surface hybridized immediately. A comparison with the control strand suggests that ~4% of these events were actually due to

incidental RET. The remaining 69% of complementary target molecules adsorbed nonspecifically on the surface and did not initially engage in RET with an immobilized probe molecule. Of these nonspecifically adsorbed molecules, only 7% executed a successful search and hybridized (~1% of those species were incidental RET events as indicated by the control experiments), with the remaining 93% desorbing prior to hybridization. Similarly, the melting of surface-bound DNA favored melting into solution (77%) over melting to the surface (23%). Molecules that melted onto the surface could then either rehybridize or, in the case of an unsuccessful search, desorb into solution and perform a three-dimensional diffusive trajectory (potentially including a large lateral displacement) prior to readsorption and a renewed search for a complementary strand.

The search and exploration process described above suggests that hybridization efficiency depends on a complex mixture of the adsorption rate from solution, the surface mobility of target molecules, the surface residence time of adsorbed target molecules, the effectiveness of collisions (*i.e.*, the fraction of collisions that lead to hybridization), and the rate of dsDNA melting in the presence of a given surface chemistry. It is interesting to consider these phenomena in the context of previous observations of DNA hybridization at surfaces. For example, Chan *et al.* found that an increased surface density of immobilized probe molecules on the surface could actually decrease the efficiency of hybridization.[17] This was interpreted as being due to reduced hybridization efficiency caused by overcrowding; our observations suggest that other factors could be at work, including the influence of DNA surface density on the mobility and desorption of nonspecifically adsorbed target. It was previously reported that ssDNA surface dynamics were strongly influenced by the physicochemical properties of a surface, including hydrophobicity.[28] In particular, ssDNA strands exhibited shorter residence times on hydrophobic surfaces, potentially influencing the time intervals associated with two-dimensional searches for a complementary strand. Hydrophobic surfaces were also shown to increase the rate of hybridization and to slow the rate of melting for DNA hairpins.[9] These observations suggest that an optimal surface chemistry would enhance the hybridization efficiency of nonspecifically adsorbed molecules, potentially by improving the search process, while simultaneously stabilizing the hybridized state. Follow-on work will further explore this possibility by carefully controlling (and varying) the chemistry of the surface "matrix" surrounding the immobilized ssDNA. The results of single-molecule TIRF-RET experiments on these surfaces will provide insight into the effects of surface chemistry (*e.g.*, surface hydrophobicity) on the mechanisms of hybridization at the solid–liquid interface

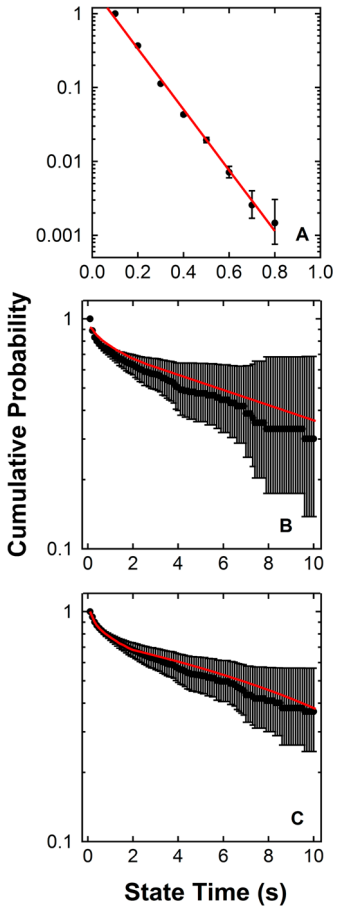

Figure 5. Cumulative state time distributions for complementary target molecules (●) and fits as described in the text (red lines). (A) Transition from searching state to hybridized, (B) desorption from hybridized state, (C) transition from hybridized to searching state.

Time Intervals of Searching and Hybridized States: Search Times and Melting Kinetics. In addition to revealing the different mechanisms associated with surface hybridization and melting, a detailed analysis of molecular trajectories also provided kinetic information about search and melting processes. In particular, each state time for a given molecule was determined by counting the number of frames the molecule remained either hybridized or searching before transitioning to the opposing state or into solution. Trajectories for each transition were accumulated to prepare cumulative state time distributions. Each distribution was fit with 1–3 exponentials; the number of exponentials was selected *via* the maximum entropy method as described in the Experimental Details. From these fits the characteristic state time and associated population fraction were extracted. Figure 5 shows cumulative probability distributions for time intervals associated with specific transitions. The data presented in Figure 5a, for example, provide statistical information about the time intervals associated with the searching state. Figure 5a comprises all searching events including those molecules that had melted and initiated a

new search of the surface. In particular, the graph shows, on a semilogarithmic scale, the fraction of molecules that search the surface for time *t* or longer. Similarly, Figure 5b and c show the fraction of molecules remaining in the hybridized state for time *t* or longer, before apparently melting into solution (Figure 5b) or onto the surface (Figure 5c), respectively. In Figure 5, the solid circles represent data from experiments using complementary target ssDNA (at 293 K), and the red lines indicate fits to one or more exponentials as described above and in more detail in the Experimental Details. The parameters resulting from these fits are given in detail in the Supporting Information (Table S1).

On the semilogarithmic plots in Figure 5, a straight line would indicate first-order kinetics; any observed deviation from this behavior therefore suggests the presence of multiple populations with distinct characteristic state times. The search time distribution (Figure 5a) shows a linear dependence on the semilogarithmic axes, and the majority of molecules searched for only fractions of a second before hybridizing; 99.9% of all observed molecules that hybridized did so in <1 s. This suggested that the local two-dimensional search for a proximal complementary strand was a rapid process. Using the maximum entropy method outlined in the Experimental Details, a single-exponential fit was found to be appropriate, and the best fit characteristic search time was determined to be 0.111 ± 0.001 s.

Once a molecule had hybridized, the transition to either the searching or in-solution state was slow by comparison to the search process. This is indicated by the relatively high probability of long state times in the cumulative hybridized state time distributions (Figure 5b,c). These distributions were clearly nonlinear on the semilogarithmic axes and exhibited long tails extending to time intervals of >10 s. The distribution describing melting into solution (Figure 5b) required a sum of three exponential functions (three melting modes) for a satisfactory fit, while the distribution describing melting onto the surface (Figure 5c) was fit with two melting modes. For these two melting processes, the two primary modes of melting had similar time scales (~15 s for slow mode and ~1.4 s for the fast mode), suggesting that the kinetics of DNA melting was independent of destination. The distribution describing melting into solution also exhibited a third transient mode with a very short characteristic state time of ~0.1 s. As shown in Figure 6, a similar state time analysis using the poly-A control target revealed a single characteristic time of ~0.1 s, suggesting that this short-lived mode represented the dissociation of a transient nonspecific interaction between ssDNA strands as opposed to actual melting of hybridized strands. Other state time distributions for the control target are shown in the Supporting Information, Figure S4.

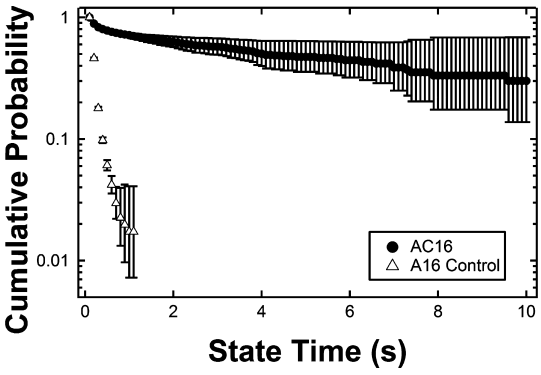

Figure 6. Cumulative hybridized state time distributions for complementary poly-AC target (●) and the poly-A control (Δ).

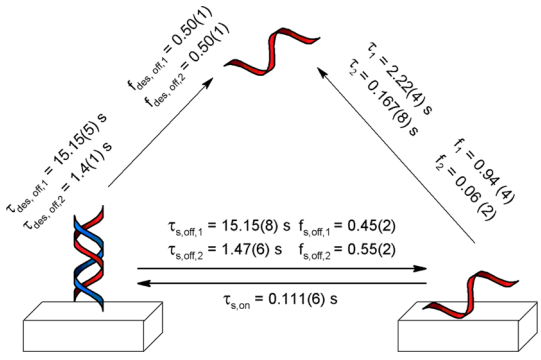

Figure 7. Characteristic state times for the pathway to surface hybridization.

All state time distributions were fit to multiple exponentials, as described in the Experimental Details, to determine the characteristic state time and fraction of each population. The most relevant parameter values from the fits are given in Figure 7 with their associated physical interpretation (see Table S1 in the Supporting Information for further detail). As mentioned previously, the search time distribution (*i.e.*, the search time interval distribution) was well described by a single exponential with a characteristic time of only 0.111 ± 0.001 s. This rapid search time suggested that molecules that adsorbed to the surface performed a brief two-dimensional search for a complement strand. If a complementary strand was not encountered quickly, the molecule desorbed and executed a three-dimensional trajectory before repeating the process. Using a typical mean diffusion coefficient determined for a model hydrophilic surface[25] (0.18 $\mu m^2/s$), it was estimated that a characteristic search distance to hybridization was approximately 0.08 μm; that is, a target molecule must adsorb within 80 nm of an immobilized probe molecule to have a high probability of hybridization. If hybridization did not occur, the target molecule desorbed from the surface with a characteristic time scale of ~2 s.

The only state time distribution found to have significant temperature dependence was the distribution

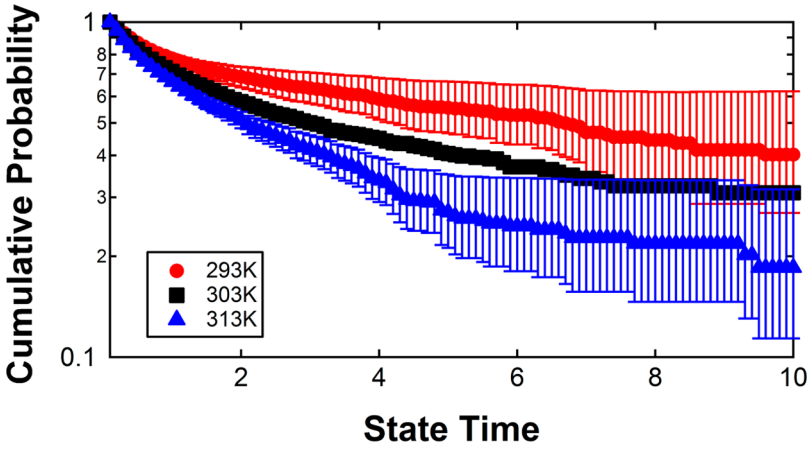

Figure 8. Semilogarithmic plots of the cumulative hybridized state time distributions for poly-AC targets at 293 K (red ●), 313 K (■), and 323 K (blue ▲).

associated with the melting of the hybridized state. Figure 8 shows cumulative hybridized state time distributions as a function of temperature. Consistent with general expectations for DNA melting, the probability of long hybridized time intervals decreased systematically with increasing temperature. This was expected, because as the temperature approached the solution melting temperature (~323 K, salt adjusted), hybridization events were expected to be less stable and exhibit shorter state times. Again, characteristic state times and population fractions were extracted through (multi)exponential fits (see Supporting Information Table S1 for details). Interestingly, while the state time corresponding to the shorter-lived hybridized state was insensitive to temperature (remaining at ~1.5 s), the characteristic state time of the longer-lived hybridized state decreased systematically from ~15 s to ~8.3 s as the temperature increased from 293 K to 313 K. This systematic decrease was consistent with expectations close to the bulk melting temperature, providing the first hint that the longer-lived "hybridized" population may be an accurate representation of the nominal DNA duplex state, while the anomalous behavior of the shorter-lived state suggests that these transient associations may not represent true (or complete) hybridization. An Arrhenius analysis of the longer-lived hybridized mode revealed that melting to the surface exhibited an apparent activation energy of E_a = 23 kJ/mol and melting into solution an apparent activation energy of E_a = 22 kJ/mol. The Arrhenius plots used in these calculations are found in the Supporting Information (Figure S5). These values are somewhat smaller, but on the same order of magnitude, as those reported in the literature for similar length strands in solution, ~40 kJ/mol.[29,30] These considerations are discussed in greater detail below, where a correlation between hybridized state time and structural parameters is described.

Melting Modes Correspond to Distinct Structural States of Association. We hypothesized that the two observed

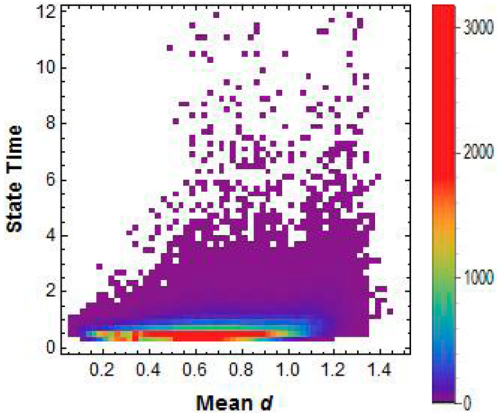

Figure 9. Heat map of state time *versus* mean *d* for every observed hybridization event. The legend to the right depicts color associated with counts of molecules in each bin.

modes of melting, with characteristic time scales of 1.4 and 15 s, respectively, might correspond to distinct states of association. Accordingly, the trajectory data were mined to identify possible correlations between the mean value of *d* for a given hybridized state and the time interval of that hybridized state. These data are presented in Figure 9 in the form of a heat map. It is visually apparent that there is a strong correlation between hybridized states with small values of *d* and states with short time intervals. For example, the vast majority of hybridization events with $d < 0.4$ exhibit state times shorter than 3 s, while hybridization events with $d > 0.4$ often remain hybridized for much longer time intervals.

To make this distinction even more apparent, Figure 10 shows cumulative hybridized state time distributions for two populations that are apparent in Figure 9 as ranges of *d* ($d < 0.4$ and $0.4 < d < 1.2$) and fit with a number of exponentials selected by the maximum entropy method. As expected from the heat map in Figure 9, the two distributions varied significantly, with the small *d* distribution decaying much more rapidly. The small *d* distribution was well described

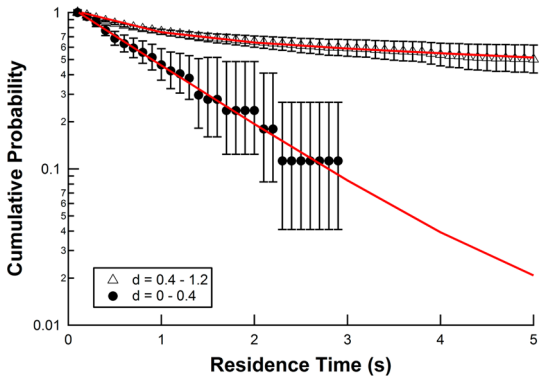

Figure 10. Cumulative hybridized state time distributions for poly-AC targets with mean d < 0.4 (●) and mean d > 0.4 (Δ).

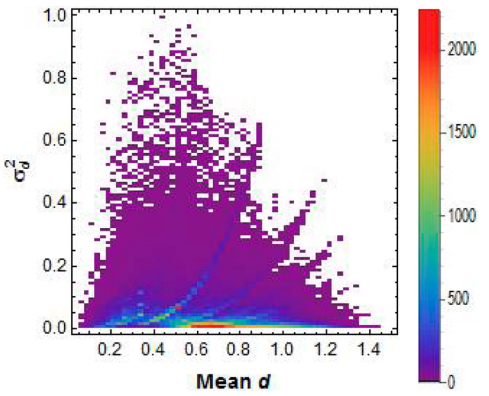

Figure 11. Heat map of variance in d *versus* mean d for every observed hybridization event. The legend to the right depicts the color associated with counts of events in each bin.

by a single exponential with a characteristic melting time of 1.9 ± 0.3 s, similar to that of the fast melting mode determined from the overall hybridized state time distribution. The large d distribution was described by a sum of two melting modes, including a dominant mode with a characteristic time constant of 16.3 ± 0.4 s, similar to that of the slow mode determined from the overall hybridized state time distribution. The large d distribution also exhibited a small fraction of melting events with a characteristic time constant of ∼0.1 s, which was attributed to the dissociation of nonspecific interactions as discussed earlier. Thus, the two melting time constants that were determined from fitting the overall hybridized state time distribution can be attributed to distinct populations that were identified on a structural basis, *i.e.*, their mean d value. While this correlation is interesting, the specific details are initially somewhat surprising, since one might intuitively expect that hybridization events that exhibit small values of d might be more strongly associated and remain associated longer; instead, the opposite was observed.

Clearly the mean d value associated with a given apparent hybridization event is not necessarily the only relevant structural parameter. In particular, one might expect that structural fluctuations might influence the likelihood of melting. Therefore, the trajectory data were analyzed to identify possible correlations between the mean value of d for a given hybridized state and the variance in d during that hybridized state (as a measure of the degree of fluctuations). These data are presented in Figure 11 in the form of a heat map. Interestingly, the data clearly show that hybridized states with small mean values of d exhibit significantly larger fluctuations than hybridized states with larger values of mean d. This is again somewhat counterintuitive structurally, but totally consistent with the fact that the large d population is much longer-lived than the small d hybridized states.

As discussed earlier, based on our estimates of the Förster radius and the molecular geometry, a nominal hybridized state is expected to have a mean value of d = 0.9 and a variance σ^2 = 0.1. Therefore, it was hypothesized that the large d population, which is long-lived (∼15 s), corresponds to this nominal hybridized state. The appearance of two modes of melting, from two distinct states, was intriguing and somewhat unexpected. In an attempt to characterize the driving forces behind this phenomenon, several hypotheses were proposed. For example, the short "hybridization" times, low d values, and large variance associated with the false hybridization mode could possibly be explained by nonspecific interactions between just the donor and acceptor fluorophores. However, this hypothesis was inconsistent with the results of the negative control experiments using the noncomplementary poly-A probe DNA, which did not exhibit this behavior. In particular, the poly-A control exhibited only a single extremely short-lived "hybridization mode" (∼200 ms), in contrast with the characteristic state time of ∼2 s for the "false" hybridization mode of the complementary probe. Alternatively, it is possible that the false hybridization mode could represent a hybridization state where the molecule is periodically zipping and unzipping the base pairs near the end of the strands. This hypothesis satisfies the observed high variance in the short hybridization mode, but fails to account for close average proximity of fluorophores indicated by the low mean value of d (high E) in this mode. A final possibility for the false hybridization mode involves an alternative specific secondary structure, *e.g.*, mismatched hybridization or another mode of coordination. It is difficult to picture how this would lead to extremely close association of fluorophores (*i.e.*, small d); however, it cannot be ruled out entirely as a possibility. A structural picture of the small d population is somewhat difficult to define, and we hesitate to speculate too broadly. What can be said with certainty is that this population represents associations between complementary ssDNA, in the near-surface region, that exhibit a small mean donor−acceptor distance with

large fluctuations. This leads to much shorter contact times than observed for the nominal hybridized state.

CONCLUSIONS

Single-molecule tracking has provided a unique opportunity to probe the effects of surface chemistries on the pathway to hybridization in an environment that is relevant to nucleic acid assays such as DNA microarrays. Unique information is accessible, providing insight into the presence of distinct molecular populations and pathways associated with hybridization and melting in the near-surface region. The experiments performed here revealed that surface-mediated DNA hybridization occurred *via* a search process that involved a complex combination of two- and three-dimensional mobility. Furthermore, information was obtained about the kinetics of melting and rehybridization. The presence of these competing processes suggested that surfaces may be defined to optimize hybridization efficiency and the stability of the hybridized state, and the data presented here provide initial design principles for such surfaces.

EXPERIMENTAL DETAILS

Materials. 3-Glycidoxypropyltrimethoxysilane (95% pure) was obtained from Gelest; *n*-butylamine (99.5% pure) was obtained from Sigma-Aldrich; Micro 90 cationic detergent was obtained from International Product Corp. All other chemicals were Optima grade from Fisher Scientific. All chemicals were used as received without further purification or modification. Aqueous solutions were prepared with water purified to 18 MΩ·cm using a Millipore Milli-Q UV+ system. The target molecule (introduced into solution) was an oligonucleotide with the sequence 5′-ACAACCAACACACCA-3′ (poly-AC, Invitrogen) with the 5′ end modified with AlexaFluor 488 dye *via* C6-Amino linker (Figure S6, top molecule). The probe molecule (attached to the surface) was an oligonucleotide with the sequence 3′-TGTTGGTTGTGTGGT-5′ (poly-TG, Biosearch) labeled with Quasar 670 dye *via* 3′ C7-Amino linker on the 3′ end and with an C6-Amino linker on the 5′ end (Figure S6, bottom molecule). The chemical structure of both probe and target oligonucleotides can be found in the Supporting Information (Figure S6). An oligonucleotide with the sequence 3′-AAAAAAAAAAAAAAA-5′ (poly-A, Invitrogen) with a 5′ AlexaFlour 488 label attached by a C6-Amino linker was used as a target in control experiments. DNA solutions were prepared in Milli-Q water to concentrations of 10^{-10} M to achieve low enough surface densities for single-molecule experiments. Amine-modified poly-TG DNA solutions were prepared in 1× PBS to concentrations of 10^{-8} M to achieve appropriate surface coverage of covalently attached DNA.

Surface Preparation. Fused silica (FS, Mark Optics) wafers were washed in a 2% Micro 90 solution and manually scrubbed with a Kim-wipe prior to rinsing with ample amounts of Milli-Q water. The wafers were then rinsed with 2-propanol and dried with ultrapure nitrogen. The wafers were subsequently placed in a piranha solution (3:1 sulfuric acid/hydrogen peroxide) at approximately 70 °C for 1 h followed by copious washing with Milli-Q water and drying with ultrapure nitrogen. The dry wafers were then treated with UV-ozone for 1 h. After the UV-ozone cleaning, 3-glycidoxypropyltrimethoxysilane (GPTMS) was used to deposit a monolayer on the FS wafers.

To form GPTMS monolayers *via* vacuum-assisted vapor deposition, a 1:2:20 solution by volume of *n*-butylamine/GPTMS/toluene was placed in the bottom of a desiccator. The FS sample was placed in a custom holding tray in a desiccator, which was then sealed and evacuated. The deposition occurred over 16−20 h at room temperature. The deposition time was selected based on systematic characterization using contact angle and ellipsometry (Supporting Information Figure S7).

To modify surfaces with immobilized ssDNA, GPTMS surfaces were prepared as described in the Experimental Details. Surface quality was verified with ellipsometry and contact angle before depositing the amine-modified poly-TG DNA. High-quality GPTMS samples were incubated for 24 h in a 1× PBS solution of 100 nM poly-TG DNA with the pH adjusted to 8−10. At the end of the deposition samples were rinsed consecutively with toluene, acetone, 2-propanol, and Milli-Q water. Following the rinsing samples were placed in a hot water bath at ∼353 K for 15 min to ensure only covalently attached ssDNA remained on the surface.

Contact-Angle Measurements. Contact angles (CA) of all surfaces were measured with a custom-built contact-angle goniometer. A 1 μL drop of Milli-Q water was deposited on the surface in seven random locations on three separate samples; the averaged values and standard deviations are reported. For unmodified FS samples, almost complete wetting of the surface was observed (CA < 5°). The CA for GPTMS was 54 ± 3° corresponding to a complete monolayer, measured by ellipsometry as discussed below.[31]

Ellipsometry Measurements. Variable-angle spectroscopic ellipsometry (J.A. Woollam, Lincoln, NE, USA) was used to measure the thickness of silane thin films in air to assess the monolayer quality. For ellipsometry experiments, 2 in. intrinsic silicon wafers (WRS Materials) were used as substrates for the thin film deposition described previously; the native oxide on these wafers is expected to be chemically similar to fused silica. An isotropic three-interface optical model consisting of air, GPTMS, native silicon dioxide, and silicon was used to fit the change in amplitude (Ψ) and change in phase (Δ) of the polarized light measured at angles from 60° to 80° at 5° intervals, spanning the spectroscopic range from wavelengths of 400 nm to 900 nm.[32] The layer thickness of GPTMS was 0.9 ± 0.1 nm, which is similar to both the fully extended molecular length and previously reported values.[15]

Total Internal Reflection Fluorescence Microscopy Measurements. A custom-built prism-based microscope composed of a Nikon TE-2000 microscope with a 60× water immersion objective was used to perform total internal reflection fluorescence microscopy measurements. A 491 nm DPSS laser was oriented to produce a TIRF field when both flow cell and prism were mounted on the microscope, the configuration of which was described in detail previously.[12] The intensity of the illumination was adjusted to permit single-fluorophore observation with a 100 ms acquisition time during sequential imaging, while also allowing continuous observation for several minutes without photobleaching.[28] Movies were 1200 frames in length (120 s), six movies were taken per sample, and experiments were run in triplicate. An Optosplit II image splitter (Cairn Research) was used for dual channel imaging. This device split the image *via* a 610 nm dichroic mirror; the dual images were then filtered by band-pass filters optimized for the AlexaFluor-488 and Quasar-670 dyes. The donor channel (Alexa-488) used a band-pass filter centered at 529 nm with a 90% transmission width of 28 nm, and the acceptor channel used a bandpass filter centered at 630 nm with a 90% transmission width of 50 nm. The two output channels were captured using an EMCCD camera cooled to −70 °C (Photometrics). The two channels were manually aligned, *via* alignment grid, to within 1−2 pixels. Images were further aligned during postprocessing by convolving the two channels as described previously by Kastantin *et al.*[27] Both poly-AC complementary target ssDNA and poly-A control ssDNA experiments were observed at temperatures of 293, 303, and 313 K using a temperature-controlled stage. All objects that resided on the surface for less than one frame (100 ms) were

removed from the data pool, as it was impossible to accurately measure state times of objects that resided on the surface for less than one frame.

Surface Coverage of Immobilized ssDNA. TIRFM was used to measure the surface density of immobilized probe ssDNA. For surface density experiments, serial dilutions of amine-modified poly-TG DNA were prepared ranging from 100 nM to 100 pM. GPTMS surfaces were prepared and incubated in each dilution. After rinsing and hot water bath the samples were examined with TIRFM, and the immobilized ssDNA was directly excited with a 643 nm wavelength laser. Images were taken with 1 s acquisition times, and individual ssDNA molecules were identified as diffraction limited objects. The number of immobilized ssDNA molecules was counted, and the image intensity was integrated to get the total intensity of each image. Over 20 locations were examined on each sample, and experiments were run in triplicate for each dilution. Using the collected data a calibration plot of intensity *versus* surface density was prepared. At greater surface densities of ssDNA it became impossible to identify individual molecules. Therefore, assuming that linearity was retained, the calibration plot was extrapolated to higher total intensities to extract an estimated surface density of ssDNA. For samples prepared using the 100 nM ssDNA concentration, the grafting density of ssDNA was estimated to be $\sim 1.5 \times 10^9$ DNA/cm^2, which equates to an average separation of ~300 nm between immobilized ssDNA strands.

Resonance Energy Transfer. Spatial information in fluorescence imaging was acquired *via* resonance energy transfer. This technique involves the nonradiative energy transfer from a donor fluorophore (Alexa-488) to an acceptor fluorophore (Quasar-670) that occurs when the two fluorophores are within 1−10 nm,[24] where the specific distance dependence is characteristic of the specific RET pair. For RET to occur, the emission spectrum of the donor fluorophore (Alexa-488) must have significant overlap with the excitation spectrum of the acceptor fluorophore (Quasar-670). The spectral overlap integral and relative orientation of the fluorophores can be combined with the optical properties of the medium to calculate the Förster radius (R_0).[24] This radius is the distance where the nonradiative energy transfer between donor and acceptor fluorophores is 50%.[33] The Förster radius for the Alexa-488/Quasar-670 RET pair is approximately 5.4 nm; the exact value is dependent on the molecular orientation (κ^2) and medium conditions (n).[34] The Förster radius coupled with the experimentally observed fluorescence intensity of the donor (F_D) and acceptor (F_A) can be used to calculate the spatial separation of the RET pair:

$$r = R_0 \left(\frac{F_{A,\, r \to 0}}{F_{D,\, r \to \infty}} \right)^{1/6} \left(\frac{F_D}{F_A} \right)^{1/6} \quad (1)$$

The ratio of acceptor fluorescence at zero separation and donor fluorescence at infinite separation is expected to be on the order of unity. Due to the uncertainty in this assumption, as well as those described above, it is challenging to calculate an exact value for r during RET experiments. Therefore, the relative distance between donor and acceptor fluorophore (d) was used to characterize DNA hybridization events.[27]

$$d = \left(\frac{F_D}{F_A} \right)^{1/6} \quad (2)$$

The relative distance d is directly related to the RET efficiency through the expression

$$E = \frac{1}{1 + d^6} \quad (3)$$

While the RET signal can be equally well described using either d or E, we have chosen to express our data in terms of d. As a quantity that is proportional to the physical donor−acceptor separation, d provides a degree of physical intuition not given by E. Moreover, in graphical representations of data, the use of d provides enhanced sensitivity to extreme values (low and high) of RET, which would be difficult to visualize if represented in terms of E.

Donor Bleeding and Direct Acceptor Excitation. A common artifact of two-channel fluorescent imaging, known as bleeding, involves a small amount of donor emission that may appear in the acceptor channel. This can be reduced to extremely low levels by appropriate selection of dichroic mirror and band-pass filters. To assess the effects of bleeding on the experiments, a control experiment was conducted using donor-labeled target ssDNA with unlabeled complementary probe ssDNA covalently attached to a GPTMS surface. These experiments exhibited strong fluorescence in the donor channel with signals below the noise threshold in the acceptor channel. Therefore, all fluorescence in the acceptor channel can be attributed to RET or to direct excitation of the acceptor fluorophore.

Direct acceptor excitation occurs when the excitation laser (meant to excite the donor to initiate RET) excites the acceptor fluorophore directly with low efficiency, causing the molecule to fluoresce in the absence of RET. To assess the effects of direct excitation, a control experiment was performed using unlabeled target ssDNA and acceptor-labeled immobilized probe ssDNA. Using the filters described previously, no fluorescence above background levels was observed in either the acceptor or the donor channel. These control experiments indicate that the system and experimental design limited direct excitation and bleed-through to levels below the noise threshold.

Nonspecific Resonance Energy Transfer. While RET between donor-labeled target and acceptor-labeled probe was intended to indicate a hybridization event, it was expected that some nonspecific target−probe interactions would also occur.[35] To characterize these nonspecific interactions, a control experiment was performed using the donor-labeled poly-A target (which was not complementary to the acceptor-labeled immobilized probes) in place of the complementary target poly-AC strands. As described below, the analysis of these data was used to characterize the spectral and dynamic signatures of false hybridization populations.

Data Analysis. Diffraction-limited objects were identified in each channel on a frame-by-frame basis using a disk matrix and thresholding algorithm.[36] For each frame, both channels were convolved to identify objects in the same position. An object's location was identified using center-of-intensity calculations. The total fluorescence intensity of each object was determined by integrating the intensities of all pixels associated with the object and subtracting the local median background intensity. An object that appeared within 3 pixels (681 nm) in consecutive frames was identified as the same object for purposes of tracking. Figure 1 illustrates the process used to identify RET events that indicated hybridization. Objects simultaneously identified within 2 pixels (455 nm) in both donor and acceptor channels were identified as RET events (Figure 1, top). The position of a RET event was identified using the channel with greatest signal-to-noise ratio. Fluoroscence intensity was monitored in both channels for each molecular trajectory (Figure 1, middle). These intensities were used to calculate the relative distance between fluorophores, d, using eq 1 on a frame-by-frame basis. As described below, trajectories were segmented into "searching" and "hybridized" time intervals for the statistical analysis of searching, hybridization, and melting kinetics.

In cases of extremely strong or extremely weak energy transfer, the intensity of a given object was high in one channel but below the noise threshold in the opposing channel. In these cases, the position of the identified object from the strong channel was applied to the weak channel to determine the effective intensity of the object in the weak channel. These objects were tracked as described earlier using a 3 pixel (681 nm) identification radius. At least 100 000 molecular trajectories were obtained for the target and control molecule on the surface. Only objects that were directly observed to both adsorb and desorb were used in the analysis to reduce uncertainty with respect to the surface state times. A given surface state time of each object (*e.g.*, searching or hybridized) was calculated as the number of frames in which the object was identified in that state multiplied by the acquisition time (100 ms). Since an object may not reside in the initial and/or final frames for the entire exposure time of that frame, the uncertainty in a given state time interval was taken to be the exposure time divided by $\sqrt{2}$.

Cumulative state time distributions were created by accumulating trajectories and examining the time spent hybridized

or searching for a complementary strand within each trajectory. Time steps in the hybridized state were identified by a high RET efficiency (*i.e.*, low *d*). The number of time steps taken before hybridization was multiplied by the acquisition time (100 ms) to determine the searching time interval. State-time distributions were created by accumulating these time intervals for all observed hybridization and searching events. Similarly, this analysis can identify searching intervals by a low RET signal (high *d*) and used to create the cumulative search time distribution. The error for each data point in the distribution represents a 68% confidence interval for a Poisson distribution.

The cumulative state time distributions were modeled using a multiexponential function, where the coefficient of each term represents a population fraction (f_i) and the time constant represents the characteristic state time (τ_i) of that population.

$$p(t) = \sum_i f_i e^{-t/\tau_i} \quad (4)$$

The number of exponentials used in the fit was determined *via* the maximum entropy method.[37] The maximum entropy method is a model-independent method that utilizes Laplace transforms to invert a distribution into a spectrum of characteristic rates.[38,39] Discrete peaks were identified in this rate spectrum and enumerated to determine the appropriate number of populations to use when applying eq 4 in a given analysis. This process has been employed to identify modes of DNA surface dynamics[28] and conformations[27] in surface residence time distributions. Mean state times were calculated by a weighted average of the characteristic state times (τ_i, determined from the fit to eq 4) of all observed populations. A more detailed discussion of this analysis was given previously.[40]

Molecular trajectories and portions of trajectories were partitioned, based on the history of each molecule, to acquire a picture of the pathways of surface-mediated DNA hybridization. As one example, each trajectory was scanned for the presence of at least one hybridization event, identified by a transition from a frame with high relative donor−acceptor distance (*d*) to a low *d* in a subsequent frame (Figure 1). The specific threshold used for this analysis is described above in greater detail. From this, the fraction of molecules that hybridized during the course of their trajectories on the surface was determined. Further analysis was performed upon this hybridizing fraction. For example, the set of trajectories that hybridized at some point during their trajectories was subpartitioned into trajectories that hybridized immediately upon adsorption (indicated by a high RET efficiency in the first observed frame) and trajectories where hybridization occurred after nonspecific adsorption. Various other populations were isolated by monitoring trajectories and changes in the relative distance between donor and acceptor fluorophores, to develop a picture of the mechanistic pathways associated with DNA hybridization in the near-surface region.

Each molecular trajectory was split into periods spent hybridized or searching for a complementary strand. These trajectory fractions were counted to determine the total number of hybridized-state events and searching-state events. The hybridized-state and searching-state events were further categorized based on the transition to a subsequent state or from a preceding state. For example, a hybridized molecule could melt either into solution (simultaneous melting and desorption) or to the searching state (unhybridized surface-bound molecules). Using melting into solution as an example of categorization by subsequent state, the number of molecules that melted into solution was divided by the total number of hybridized-state events to acquire the fraction of melting events that involved melting into solution. As an example of categorization by previous state, the number of molecules that melted into solution was divided by the total number of molecules that desorbed, providing the fraction of desorbed molecules that came from the melted state. Using this approach, the fractions of molecules in each state that transitioned to or from either of the other states were determined. This is clearly demonstrated in the Results and Discussion section.

The fractional pathway analysis was adjusted to account for the finite time resolution of the experiments. Without this adjustment, certain pathways (*i.e.*, those originating in adsorption or ending in desorption) would be undercounted. For example, below the time resolution it is impossible to distinguish between a molecule that hybridized directly upon adsorption from solution and a molecule that adsorbed nonspecifically but hybridized quickly so that the search time could not be resolved. To compensate for this limitation, an adjustment was performed using cumulative distributions of time intervals associated with the relevant state for these transitions. Specifically, a given state time distribution was extrapolated backward to a state time of 0 s using parameters determined in the fitting process described above. The fraction of molecules missed was then determined by integration from 0 to 0.1 s (the approximate time resolution of the experiment). This fraction was then used to adjust the fraction of molecules that underwent a transition, *i.e.*, melting into solution.

Conflict of Interest: The authors declare no competing financial interest.

Acknowledgment. The authors gratefully acknowledge support for D.K.S. and J.H.M. from the National Institute of Biomedical Imaging and Bioengineering of the National Institutes of Health (5R21EB015061-02). Additional support was provided by the National Science Foundation (award CHE-1306108) for D.K.S. and for the development of single-molecule RET tracking methods. We also thank M. Kastantin for his invaluable assistance.

Supporting Information Available: The structure of both labeled complementary strands used in this work is shown. Additionally, the *d* distribution for the poly-A control experiments is provided. The sensitivity analysis of the hybridization threshold is presented and discussed. A comparison of the cumulative state time distributions for both the poly-AC probe and poly-A control is shown for all transitions between states. The Arrhenius analysis of the melting to the surface and into the solution for the nominal hybridization mode is shown. Lastly, the temperature dependence of both the fractional pathway to hybridization and the characteristic state times is shown. This material is available free of charge *via* the Internet at http://pubs.acs.org.

REFERENCES AND NOTES

1. Graves, D. J. Powerful Tools for Genetic Analysis Come of Age. *Trends Biotechnol.* **1999**, *17*, 127–134.
2. Hacia, J. G.; Brody, L. C.; Chee, M. S.; Fodor, S. P.; Collins, F. S. Detection of Heterozygous Mutations in Brca1 Using High Density Oligonucleotide Arrays and Two-Colour Fluorescence Analysis. *Nat. Genet.* **1996**, *14*, 441–447.
3. Wang, D. G.; Fan, J. B.; Siao, C. J.; Berno, A.; Young, P.; Sapolsky, R.; Ghandour, G.; Perkins, N.; Winchester, E.; Spencer, J.; *et al.* Large-Scale Identification, Mapping, and Genotyping of Single-Nucleotide Polymorphisms in the Human Genome. *Science* **1998**, *280*, 1077–1082.
4. Cutler, D. J.; Zwick, M. E.; Carrasquillo, M. M.; Yohn, C. T.; Tobin, K. P.; Kashuk, C.; Mathews, D. J.; Shah, N. A.; Eichler, E. E.; Warrington, J. A.; *et al.* High-Throughput Variation Detection and Genotyping Using Microarrays. *Genome Res.* **2001**, *11*, 1913–1925.
5. Chee, M.; Yang, R.; Hubbell, E.; Berno, A.; Huang, X. C.; Stern, D.; Winkler, J.; Lockhart, D. J.; Morris, M. S.; Fodor, S. P. Accessing Genetic Information with High-Density DNA Arrays. *Science* **1996**, *274*, 610–614.
6. Irving, D.; Gong, P.; Levicky, R. DNA Surface Hybridization: Comparison of Theory and Experiment. *J. Phys. Chem. B* **2010**, *114*, 7631–7640.
7. Peterson, A. W.; Heaton, R. J.; Georgiadis, R. M. The Effect of Surface Probe Density on DNA Hybridization. *Nucleic Acids Res.* **2001**, *29*, 5163–5168.
8. Wong, E. L. S.; Chow, E.; Gooding, J. J. DNA Recognition Interfaces: The Influence of Interfacial Design on the Efficiency and Kinetics of Hybridization. *Langmuir* **2005**, *21*, 6957–6965.
9. Kastantin, M.; Schwartz, D. K. DNA Hairpin Stabilization on a Hydrophobic Surface. *Small* **2013**, *9*, 933–941.

10. Okahata, Y.; Kawase, M.; Niikura, K.; Ohtake, F.; Furusawa, H.; Ebara, Y. Kinetic Measurements of DNA Hybridization on an Oligonucleotide-Immobilized 27-MHz Quartz Crystal Microbalance. *Anal. Chem.* **1998**, *70*, 1288–1296.
11. Peterson, A. W.; Wolf, L. K.; Georgiadis, R. M. Hybridization of Mismatched or Partially Matched DNA at Surfaces. *J. Am. Chem. Soc.* **2002**, *124*, 14601–14607.
12. Honciuc, A.; Harant, A. W.; Schwartz, D. K. Single-Molecule Observations of Surfactant Diffusion at the Solution-Solid Interface. *Langmuir* **2008**, *24*, 6562–6566.
13. Peterson, A. W.; Heaton, R. J.; Georgiadis, R. M. The Effect of Surface Probe Density on DNA Hybridization. *Nucleic Acids Res.* **2001**, *29*, 5163–5168.
14. Henry, M. R.; Wilkins Stevens, P.; Sun, J.; Kelso, D. M. Real-Time Measurements of DNA Hybridization on Microparticles with Fluorescence Resonance Energy Transfer. *Anal. Biochem.* **1999**, *276*, 204–214.
15. Tsukruk, V. V.; Luzinov, I.; Julthongpiput, D. Sticky Molecular Surfaces: Epoxysilane Self-Assembled Monolayers. *Langmuir* **1999**, *15*, 3029–3032.
16. Chan, V.; Graves, D. J.; McKenzie, S. E. The Biophysics of DNA Hybridization with Immobilized Oligonucleotide Probes. *Biophys. J.* **1995**, *69*, 2243–2255.
17. Erickson, D.; Li, D.; Krull, U. J. Modeling of DNA Hybridization Kinetics for Spatially Resolved Biochips. *Anal. Biochem.* **2003**, *317*, 186–200.
18. Rich, A.; Davidson, N. R.; Pauling, L. *Structural Chemistry and Molecular Biology*; W. H. Freeman: San Francisco, 1968.
19. Benichou, O.; Loverdo, C.; Moreau, M.; Voituriez, R. Optimizing Intermittent Reaction Paths. *Phys. Chem. Chem. Phys.* **2008**, *10*, 7059–7072.
20. Astumian, R. D.; Chock, P. B. Interfacial Reaction Dynamics. *J. Phys. Chem.* **1985**, *89*, 3477–3482.
21. Benichou, O.; Grebenkov, D.; Levitz, P.; Loverdo, C.; Voituriez, R. Optimal Reaction Time for Surface-Mediated Diffusion. *Phys. Rev. Lett.* **2010**, 105.
22. Millan, K. M.; Saraullo, A.; Mikkelsen, S. R. Voltammetric DNA Biosensor for Cystic Fibrosis Based on a Modified Carbon Paste Electrode. *Anal. Chem.* **1994**, *66*, 2943–2948.
23. Peterlinz, K. A.; Georgiadis, R. M.; Herne, T. M.; Tarlov, M. J. Observation of Hybridization and Dehybridization of Thiol-Tethered DNA Using Two-Color Surface Plasmon Resonance Spectroscopy. *J. Am. Chem. Soc.* **1997**, *119*, 3401–3402.
24. Lakowicz, J. R. *Principles of Fluorescence Spectroscopy*, 3rd ed.; Springer: New York, 2006.
25. Mandelkern, M.; Elias, J. G.; Eden, D.; Crothers, D. M. The Dimensions of DNA in Solution. *J. Mol. Biol.* **1981**, *152*, 153–161.
26. Mergny, J. L.; Lacroix, L. Analysis of Thermal Melting Curves. *Oligonucleotides* **2003**, *13*, 515–537.
27. Kastantin, M.; Schwartz, D. K. Connecting Rare DNA Conformations and Surface Dynamics Using Single-Molecule Resonance Energy Transfer. *ACS Nano* **2011**, *5*, 9861–9869.
28. Monserud, J. H.; Schwartz, D. K. Effects of Molecular Size and Surface Hydrophobicity on Oligonucleotide Interfacial Dynamics. *Biomacromolecules* **2012**, *13*, 4002–4011.
29. Sorgenfrei, S.; Chiu, C. Y.; Gonzalez, R. L., Jr.; Yu, Y. J.; Kim, P.; Nuckolls, C.; Shepard, K. L. Label-Free Single-Molecule Detection of DNA-Hybridization Kinetics with a Carbon Nanotube Field-Effect Transistor. *Nat. Nanotechnol.* **2011**, *6*, 126–132.
30. Banerjee, D.; Pal, S. K. Direct Observation of Essential DNA Dynamics: Melting and Reformation of the DNA Minor Groove. *J. Phys. Chem. B* **2007**, *111*, 10833–10838.
31. Igor Luzinov, D. J.; Liebmann-Vinson, A.; Cregger, T.; Foster, M. D.; Tsukruk, V. V. Epoxy-Terminated Self-Assembled Monolayers: Molecular Glues for Polymer Layers. *Langmuir* **2000**, *16*, 504–516.
32. Tompkins, H. G. *A User's Guide to Ellipsometry*; Academic Press: Boston, 1993.
33. Work, T. S.; Work, E. *Laboratory Techniques in Biochemistry and Molecular Biology*; North-Holland Pub. Co.: Amsterdam, 1969.
34. Sahoo, H. Förster Resonance Energy Transfer - a Spectroscopic Nanoruler: Principle and Applications. *J. Photochem. Photobiol. C* **2011**, *12*, 20–30.
35. Bentley, D. R. Whole-Genome Re-Sequencing. *Curr. Opin. Genet. Dev.* **2006**, *16*, 545–552.
36. Walder, R.; Schwartz, D. K. Single Molecule Observations of Multiple Protein Populations at the Oil-Water Interface. *Langmuir* **2010**, *26*, 13364–13367.
37. Brochon, J.-C. [13] Maximum Entropy Method of Data Analysis in Time-Resolved Spectroscopy. In *Methods in Enzymology*; Michael, L. Johnson, L. B., Ed.; Academic Press: New York, 1994; Vol. Vol. 240, pp 262−311.
38. Steinbach, P. J. Inferring Lifetime Distributions from Kinetics by Maximizing Entropy Using a Bootstrapped Model. *J. Chem. Inf. Comput. Sci.* **2002**, *42*, 1476–1478.
39. Cornwell, T. J.; Evans, K. F. A Simple Maximum-Entropy Deconvolution Algorithm. *Astron. Astrophys.* **1985**, *143*, 77–83.
40. Kastantin, M. K. M.; Langdon, B. B.; Chang, E. L.; Schwartz, D. K. Single-Molecule Resolution of Interfacial Fibrinogen Behavior: Effects of Oligomer Populations and Surface Chemistry. *J. Am. Chem. Soc.* **2011**, *133*, 4975–4983.